# Optical remote sensing image apparent radiance topographic correction physical model

**SHI Di, YAN Guang-jian, MU Xi-han**

*School of Geography, Beijing Normal University, Beijing* 100875, *China*

**Abstract:** In rugged areas, topographic effects severely influence the spectrum characters of remote sensing image. Topographic correction is a necessary step to estimate real land surface situation from remote sensing images. As a kind of topographic correction methods, empirical approaches can hardly achieve desirable results. Existing physical topographic correction methods which are based on radiant transfer models require a considerable number of input parameters. Furthermore, the topographic correction and atmospheric correction are mixed, which cause inconvenience and instability. A simplified physical algorithm is proposed in this paper to overcome the disadvantages of existing algorithms. A ratio factor of diffuse irradiance on horizontal surface to solar direct irradiance is introduced. The algorithm only need solar geometry information and atmosphere model parameters as its input data, and is mainly concentrated on the removal of topographic effects. It can correct the apparent radiance of optical remote sensing images over rugged terrain to the apparent radiance without topographic effects. The algorithm was illustrated using a Landsat TM image.

**Key words:** topographic correction, apparent radiance, physical model, aerosol optical depth (AOD), 6S

**CLC number:** TP701 **Document code:** A

## 1 INTRODUCTION

Radiation corrections, such as radiation calibration, atmospheric effects removal, solar incident angle transformation and topographic effects correction should be carried out before remote sensing images were broadly applied to quantitative analysis in all fields. One of the most complex steps is topographic effects correction. Topographic effects not only cause the phenomenon that the observational targets of the same characters exhibit different spectrums or the different targets have the same spectrums, but also lead to anisotropic reflection on a pixel scale (Schaaf, 1994), which results in disadvantageous impacts for further application of remote sensing image in land classification, resource administration, mountainous-forest reserves monitoring (Collins & Woodcock, 1996; Olsson, 1995; Itten, Meyer, 1993). In China, mountainous areas accounts for 33% in the total territory of all kinds of landforms, therefore, topographic correction is particularly important for remote sensing applications.

Various topographic correction methods for remote sensing images have been investigated, which can be mainly divided into empirical models and physically based models. Empirical models are simple and practical, including the bands ratio model, principal component analysis model and regression analysis model, etc. To establish these models, a series of empirical statistical analysis were performed on the relationship between remote sensing parameters and the data from ground observations. This type of models has a strong dependence on research regions. Different models need to be generated for different areas, and the models and parameters have no specific physical meaning. Physical models are mainly built on the basis of radiant transfer equations, which quantitatively analyze radiation sources, and describe the physical processes of radiation transferred between atmosphere and land surface, to correct radiation distortions casing by topography. For instance, the model designed by Yan Guangjian which is based on light-source analysis (Yan *et al.*, 2000). Radiation sources in the models typically include three parts: direct solar radiation, sky diffuse scattering and adjacent-terrain-reflect radiation. Physical models have parameters of specific physical meanings, wide application, and are less dependent on the land type to some extent. However, physical models also have obvious disadvantages, such as, solutions of high complex equations, much more input parameters, which comparatively cause more difficulties to be used for research. Therefore, in order to solve the equations, it is necessary to ignore non-essential factors or make assumptions.

This study aims at exploring a simple correction method to remove the topographic effects. Based on mountainous radiant transfer model, the model is designed to build formula of converting mountainous terrain pixel radiance to that received on

**Received**: 2008-05-09; **Accepted**: 2009-01-07

**Foundation**: National Natural Science Foundation of China (No. 40871164), National 973 Project (No. 2007CB714402) and EU 7th Framework Program (No. 212921).

**First author biography**: SHI Di (1983— ), female,Graduated Student, Research in the realm of Optical Remote Sensing.

**Corresponding Author**: Yan Guangjian, giyan@bnu.edu.cn

flat terrain in the same condition involving the atmospheric transmittance and multiple reflections between atmosphere and land surface. Through model simplification, we ultimately achieve a relative precise terrain effect correction approach which only need a small number of parameters. To illustrate, Miyun County (Beijing) was selected as the study area, the LANDSAT-5 TM satellite images and the corresponding Digital Elevation Model (DEM) were used. After analyzing the results, we found the new topographic correction method can effectively remove the effects caused by terrains.

## 2 TOPOGRAPHIC CORRECTION MODELING

### 2.1 Mountainous radiant transfer model

The radiant interaction mechanism between radiant in mountain region and land surface is complex, and make it very difficult to solve the equations of the model. Most of previous researches are under the Lambertian surface assumption (Yan *et al.*, 2000; Franklin *et al.*, 1986; Hill & Radiometric, 1998; Richter, 1996a,1996b), as well as isotropy assumption of atmosphere scattering. For a Lambertian surface, radiance L received by sensor includes two parts: the radiance reflected by land surface and then attenuated by atmosphere and the radiance reflected by atmosphere itself (that is, path radiation), which can be expressed as:

$$L = L'\mathrm{e}^{-\tau/\cos\theta_\mathrm{v}} + L_\mathrm{p} \tag{1}$$

where, $\theta_\mathrm{v}$ is the observation zenith angle, $\tau$ is the total atmospheric optical thickness, $L_\mathrm{p}$ is the path radiance received by sensors, $L'$ is the radiance reflected by surface.

Radiance of a certain pixel comes from three parts of the effective illumination $E$ (Zhong *et al.*, 2006): $E_\mathrm{d}$ is the solar direct radiation on the ground surface; $E_\mathrm{f}$ is sky diffuse scattering on the ground surface, and $E_\mathrm{a}$ is the radiation from visible adjacent terrains. If the surface reflectance of observation direction is $\rho$, the total reflected radiance of any pixel can be expressed as $L'$:

$$L' = \rho\left(E_\mathrm{d} + E_\mathrm{f} + E_\mathrm{a}\right)/\pi = \rho E/\pi \tag{2}$$

### 2.2 The calculation of solar direct radiation

*2.2.1 Solar direct radiation*

Solar direct radiation penetrates the atmosphere and reaches the earth's surface. Incident solar energy per unit area closely relates to the geometry between radiation direction and land surface, and is functionally related to atmospheric optical thickness. Assuming that atmosphere consists of a number of uniform thin layer, then the direct incident radiation to the slope can be expressed as:

$$E_\mathrm{d} = \Theta\cos i E_0\mathrm{e}^{-\tau/\cos\theta_\mathrm{s}} \tag{3}$$

where $\Theta$ is the sheltering coefficient of terrain, if the slope is in shadow area, $\Theta$ equals to 0, otherwise it equals to 1; $E_0$ is the solar irradiance at the top of atmosphere perpendicular to the solar incidence direction; $\tau$ is the total vertical atmospheric optical thickness; $\theta_\mathrm{s}$ is solar zenith angle.

Where, the solar effective incidence angle $i$ is defined as: the angle between solar incidence ray and the surface normal, it can be calculated through Eq.(4):

$$\cos i = \cos\theta_\mathrm{s}\cos\theta_\mathrm{p} + \sin\theta_\mathrm{p}\sin\theta_\mathrm{s}\cos\left(\phi - A\right) \tag{4}$$

where, $\phi$ is the solar azimuth angle; $\theta_\mathrm{p}$ is slope gradient; and $A$ is the aspect of the slope.

*2.2.2 Sky diffuse irradiance*

Solar radiation encounter with air molecules, dusts, cloud droplets and other particles when pass through the atmosphere, and then change its path direction, spread from a particle as the center in all directions to form the sky diffuse scattering. Diffuse scattering is anisotropic distribution, influenced by the characteristics of various particles which cause scattering, and the solar incidence angle. In this article, the complex anisotropy is ignored, and we assume that sky diffuse scattering is isotropic distribution, besides, the sky view factor $V$ is introduced as the ratio of sky diffuse scattering received by a slope pixel to that on an unobstructed horizontal surface (Dozier & Frew, 1990),

$$E_\mathrm{f} = V\cdot E_\mathrm{f}^\mathrm{h}$$

$$V \approx \frac{1}{2\pi}\int_0^{2\pi}[\cos\theta_\mathrm{p}\sin^2 H_\phi + \sin\theta_\mathrm{p}\cos(\phi - A)(H_\phi - \sin H_\phi\cos H_\phi)]\mathrm{d}\phi \tag{5}$$

where, $H_\phi$ is the largest sky view angle in $\phi$ direction.

*2.2.3 Adjacent terrain irradiance*

In this paper, we ignored the impact of atmospheric absorption on the environment irradiance reflected by surrounding terrain. And according to the analysis of Proy *et al*., (1989), if assuming Lambertian on pixel level, the reflected radiation comes from each surrounding point $M$ to pixel $N$ can be expressed as $E_\mathrm{a}$ ($\mathrm{Wm}^{-2}$) in a point by point form,

$$E_\mathrm{a} = \sum_M \frac{L_M\cos T_N\cos T_M\mathrm{d}S_M}{r_{MN}^2} \tag{6}$$

where, $L_M$ expresses the radiance of the point $M$; $T_M$ and $T_N$, respectively, express angles between slope normal of point $M$, $N$ and the $MN$ connection line; $\mathrm{d}S_M$ is the actual area of pixel $M$; $r_{MN}$ is the distance between point $M$ and point $N$ (Fig. 1).

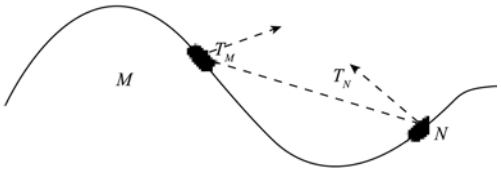


Fig. 1 Relationship of two adjacent pixels

### 2.3 Setting up of the terrain correction model

6S (Second Simulation of the Satellite Signal in the Solar Spectrum) model is a comparatively mature one of the atmospheric correction models at present, which was developed by

E.F.Vermote etc in the late nineties twenty-first century based on 5S model(Vermote *et al*., 1997), including a variety of atmospheric aerosol models such as continental type, marine type, urban type, desert background type, user-defined type, and it also provides six atmospheric models, such as mid-latitude summer, mid-latitude winter, the United States standard atmosphere, tropical atmosphere, subarctic atmosphere, subantarctic atmosphere, as well as nine bidirectional reflection models. Imitating 6S, we define the absorption transmittance for the direct radiance on the whole trip though atmosphere as $T(\theta_s, \theta_v)$, and the sun downward diffuse radiation transmission as $t_d(\theta_s)$, upward diffuse radiation transmission reflected by land surface as $t_d(\theta_v)$. Considering the multiple scattering between atmosphere and the land surface, the apparent radiance of each pixel is:

$$L = T(\theta_s, \theta_v)\left\{\frac{E}{\pi(1-\bar{\rho}S)}\left[e^{-\tau/\cos\theta_v}\rho + \bar{\rho}t_d(\theta_v)\right] + L_p\right\} \quad (7)$$

where, $S$ is the atmospheric spherical albedo, $\bar{\rho}$ is the average reflectance for underlying surface pixel, $\rho$ is the pixel reflectance. Defining sky diffuse scattering at horizontal ground level as $E_f^h$, sun direct radiation perpendicular to the received pixel as $E_i$, then the direct radiation on ground level is:

$$E_i^h = E_i \cos\theta_s = E_0 \cos\theta_s e^{-\tau/\cos\theta_s}.$$

According the definition of diffuse transmittance and the direct transmittance in 6S, we have,

$$t_d(\theta_s)/e^{-\tau/\cos\theta_s} = E_f^h/E_i^h = E_f^h/E_0\cos\theta_s e^{-\tau/\cos\theta_s} \quad (8)$$

Define the proportion of the ground level surface diffuse solar radiation and the direct radiation vertical to the surface as factor k, that is $E_f^h/E_i = k$, then:

$$t_d(\theta_s)/e^{-\tau/\cos\theta_s} = k/\cos\theta_s \quad (9)$$

Although this relationship is set up based on the ratio of sky scattering received on horizontal ground level to direct solar radiation on the observation direction, this relationship can also be used to describe the ratio between scattering radiance transmittance and direct radiance transmittance. From the analysis in the text below, $k$ changes monotonically with cosine of incident sun zenith angle and aerosol optical thickness, this means that an unique $k$ can be solved through the incident solar zenith angle cosine and aerosol optical thickness. This facilitates the simplification of the mountainous radiant equation, and even benefits atmospheric effects correction.

Radiance of any pixel received by satellite is as followed:

$$L = T(\theta_s, \theta_v)\left\{E_i\frac{\Theta\cos i + Vk + E_a/E_i}{\pi(1-\bar{\rho}S)}\times [e^{-\tau/\cos\theta_v}\rho + e^{-\tau/\cos\theta_v}\bar{\rho}k/\cos\theta_v] + L_p\right\} \quad (10)$$

Assuming the surface is absolutely flat and there is no reflection from the surrounding pixels, and the sky diffuse radiation is not blocked, the apparent radiance of this pixel is:

$$L_x = T(\theta_s, \theta_v)\left\{E_i\frac{\cos\theta_s + k}{\pi(1-\bar{\bar{\rho}}S)}[e^{-\tau/\cos\theta_v}\rho + e^{-\tau/\cos\theta_v}\bar{\bar{\rho}}k/\cos\theta_v] + L_p\right\} \quad (11)$$

As one of the mid- and high -resolution satellite sensor, TM sensor has an observation angle approximate to 0° and narrow field of view. If the observation angle is set to 0°, and the difference among $\rho$, $\bar{\rho}$, $\bar{\bar{\rho}}$ is ignored, we can get the correction model which is only used to remove topographic effects:

$$L_x = \frac{[L - T(\theta_s, 0°)L_p][\cos\theta_s + k]}{\Theta\cos i + Vk + E_a/E_i} + T(\theta_s, 0°)L_p \quad (12)$$

## 3 PARAMETERS RETRIEVAL AND CALCULATION

From the original image and DEM, we can obtain solar zenith angle, azimuth angle, the slope of each pixel, and other topographical factors. From Eq.(12), in order to correct topographic effect, $T(\theta_s, 0°)L_p$, $k$ and $E_a/E_i$ must be achieved from image or other auxiliary parameters. LANDSAT-5 TM satellite image data is applied in this article, and the observation zenith angle is assumed to be 0°. This method is also applicable to high-resolution remote sensing images with narrow field of view and nadir view geometry. The main method in this paper is to set up two types of look-up tables under different atmospheric conditions provided by 6S, and interpolate the required parameters under different atmospheric patterns.

### 3.1 Look-up tables of the atmospheric parameters

By analysis, when under fixed aerosol model and atmosphere model situations, the necessary atmospheric parameters $k$ and $T(\theta_s, 0°)L_p$ only vary with the solar zenith angle and aerosol optical thickness. Furthermore, the parameters $k$ and $T(\theta_s, 0°)L_p$ under different atmospheric models have very tiny variances, so the relationship set up in a particular atmosphere model is universal to large extent. Fig. 2 shows the variance trends of $T(\theta_s, 0°)L_p$ and $k$ with the solar zenith angle and aerosol optical thickness of TM band 1 under the continental aerosol mode. In this article, a look-up table was set up based on aerosol optical thickness, solar zenith angle with atmospheric parameters $T(\theta_s, 0°)L_p$ and $k$ (look-up Table 1) given by 6S in different aerosol mode. For each aerosol mode, the look-up table includes six aerosol optical thickness (0.05, 0.1, 0.3, 0.5, 0.7, 1), six solar zenith angles (0.71°, 16.19°, 38.45°, 46.19°, 59.81°, 67.5°). Assuming aerosol mode, aerosol optical thickness and solar zenith angle are known, atmosphere parameters can be obtained from look-up tables. Aerosol optical thickness can be resolved from dark object method. The details will be explained at Section 3.2.

### 3.2 Aerosol optical thickness

Currently, the methods of obtaining aerosol optical thickness from remote sensing images are: classified matching method,

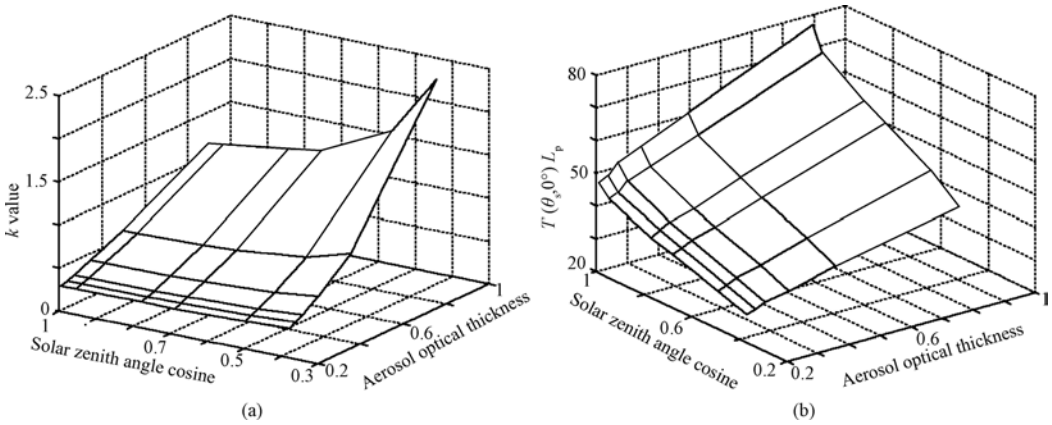


Fig. 2 Continental mid-latitude winter TM1 $T(\theta_s,0°)L_p$ and $k$ variance trends

(a) Relationship between $k$ value, solar zenith angle cosine and the aerosol optical thickness; (b) Relationship between $T(\theta_s,0°)L_p$, solar zenith angle cosine and the aerosol optical thickness

contrast estimation method, dark object method and so on (Zheng & Zeng, 2004; Wang *et al.*, 2003; Zhao, *et al.*, 2007). The dark object method proposed by Kaufman and Tanre is the most widely used retrieval method of aerosol optical thickness on land, which also achieves good results at seas, dense vegetations and the inland water regions (King *et al*., 1999; Remer *et al.*, 2005). The principle is based on the character of that 2.13μm (TM band 7) is transparent for dust aerosol particle. Thereby, without considering the characteristics of aerosol scattering, as long as we eliminate the water vapor absorption, the ground reflectance can be considered as the apparent reflectance. And the reflectance of dark objects at 2.13μm (TM band 7) has stable empirical relationship with reflectance at 0.4—0.48μm (TM band 1) and 0.6—0.68μm (TM band 3). Since apparent reflectance of dark objects have been known, after obtaining TM1 and TM3 surface reflectance, aerosol optical thickness can be calculated by interpolating look-up tables.

According to Kaufman and Tanre's method, dark object pixels are obtained one by one through retrieval process. First of all, according to the assumption of that $\rho_1$ equals 0.01 and $\rho_3$ equals 0.02, dark pixels are retrieved whose vegetation reflectance are at the range of 0.036—0.044 for TM band 7. The pixels in shaded area are removed using the sheltering coefficients of terrain. Finally, normalized difference vegetation index (NDVI) is used to determine whether the pixel is in dense vegetation area or not. Referring to empirical relationship of surface reflectance at TM band 1, band 3 and band 7, $\rho_1$ equals to $\rho_7'/4$, $\rho_3$ equals to $\rho_7'/2$, we can get the true surface reflectance of dark object at TM band 1 and 3. The aerosol optical thickness can be obtained using the apparent reflectance of these two bands and look-up table 2.

Look-up table 2 is a composite of the relationship between the solar zenith angle, the surface reflectance, the apparent reflectance and the aerosol optical thickness. Aerosol optical thickness can be interpolated from the others. During the setting up of the look-up table, the range of dark object reflection was considered. Five ground reflectance (0.005, 0.01, 0.05, 0.2, 0.5), five apparent reflectance (0.005,0.01,0.05,0.2,0.5), and six solar zenith angles (0.71, 16.19, 38.45, 46.19, 59.81, 67.5) were selected. The aerosol optical thickness of TM band 1 and band 3 were calculated through 6S. When using look-up table to calculate TM band 1 and band 3 aerosol optical thickness, other input parameters are linear interpolated between those listed above. Other bands aerosol optical thickness can be calculated in accordance with the following formula (Remer *et al.*, 2005):

$$\tau_i = a\,\lambda_i^{-b} \tag{13}$$

where, $\tau_i$ is the aerosol optical thickness of the certain band; $\lambda_i$ is the center wavelength of the band; $a$ and $b$ are Angstrom Coefficient, obtained through the pixel -by-pixel regression.

When retrieving aerosol optical thickness, the apparent reflectance of TM band 7 $\rho_Q'$ of dark object is got as follows:

$$\rho_Q' = \frac{\pi L_Q d^2}{E_0 \cos\theta_s} \tag{14}$$

where, $L_Q$ is apparent radiance of pixel $Q$, $d$ is distance between sun and earth in astronomical units of the typical date.

### 3.3 Rayleigh scattering optical thickness

Rayleigh scattering optical thickness only has small changes under different aerosol models, so it can be expressed as the same value. In addition it varies with the elevation of a pixel. With 6S, we can get Rayleigh scattering optical thickness of each band at the elevation of 0 km 1 km, and 2.5 km respectively. The relationship between TM four bands' Rayleigh scattering optical depth and the elevation can be built. As shown in Fig. 3, $\tau_{\text{raleigh}}1$、$\tau_{\text{raleigh}}2$、$\tau_{\text{raleigh}}3$、$\tau_{\text{raleigh}}4$ are Rayleigh scattering optical depth of four bands, and $h$ is the height of target pixel. The Rayleigh scattering optical thickness can then be expressed as functions of elevation.

$$\begin{aligned}
\tau_{\text{raleigh}}1 &= -0.017h + 0.165 \\
\tau_{\text{raleigh}}2 &= -0.008h + 0.085 \\
\tau_{\text{raleigh}}3 &= -0.004h + 0.046 \\
\tau_{\text{raleigh}}4 &= -0.001h + 0.017
\end{aligned} \tag{15}$$

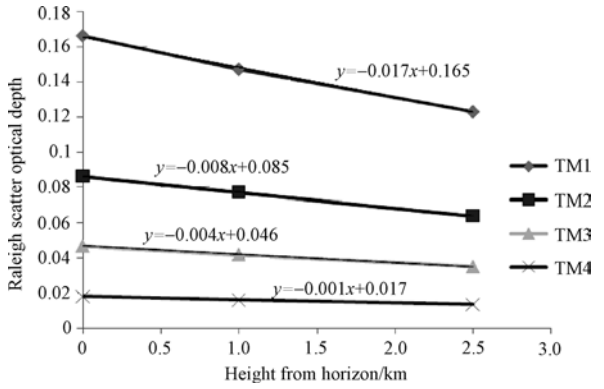


Fig. 3 Raleigh scatter optical depth

The total atmospheric optical thickness can be calculated by the following formula:

$$\tau=\tau_{\text{rayleigh}}+\tau_{\text{aerosols}} \tag{16}$$

where, the total atmospheric optical thickness is $\tau$, aerosol optical thickness is $\tau_{\text{aerosols}}$, Rayleigh scattering optical depth is $\tau_{\text{rayleigh}}$.

### 3.4 Total gaseous transmittance

The atmospheric absorption transmittance varies with solar zenith angle and elevation of the target pixel. Impacts on atmospheric total gaseous absorption transmittance of elevation at TM band 1, 2, and 3 are very small. For TM band 4, the largest bias is 6.1% when the elevation variation is less than 2.5km. As a result, in the mountainous areas below 3km, in order to calculate the total atmospheric absorption transmittance, we assume that the absorption transmittance does not vary with the change of elevation. As what is shown in Fig. 4, the relationships of the gaseous absorption transmittance and the cosine of the solar zenith angle were obtained for the first 4 bands of TM using the average value of the total gaseous absorb transmittances at sea level and 2.5km respectively:

$$\begin{aligned}
T_{g1}&=-0.152\cos\theta_s^2+0.247\cos\theta_s+0.886\\
T_{g2}&=-0.59\cos\theta_s^2+0.974\cos\theta_s+0.527\\
T_{g3}&=-0.411\cos\theta_s^2+0.677\cos\theta_s+0.668\\
T_{g4}&=-0.065\cos\theta_s^2+0.139\cos\theta_s+0.894
\end{aligned} \tag{17}$$

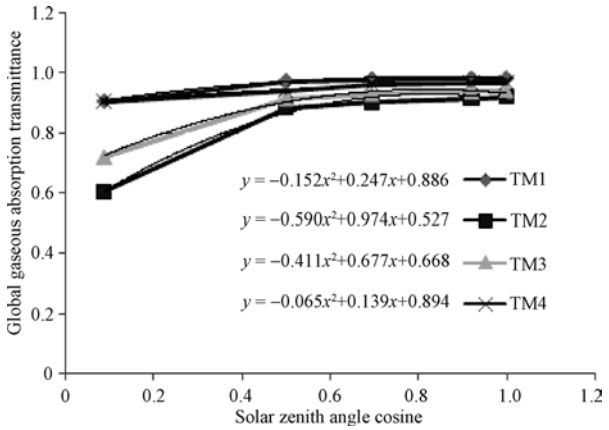


Fig. 4 Relationship between global gaseous absorption transmittance and cosine sun zenith angle

$T_{g1}$、$T_g$、$T_{g3}$、$T_{g4}$ are four bands' gaseous absorption transmittances, $\cos\theta_S$ is solar zenith cosine.

### 3.5 Adjacent terrain radiation

Eq. (18) can be obtained from Eq. (6):

$$\frac{E_a}{E_i}=\sum_M \frac{L_M\cos T_N\cos T_M\,\mathrm{d}S_M}{r_{MN}^2 E_i} \tag{18}$$

Thus, to calculate the adjacent terrain irradiance ratio $E_a/E_i$, we must first know the pixel radiance from the pixels around. In order to address this self-contradiction, we assume that the radiation received by sensors can be accurately calculated by Eq.(1), so the radiance $L_N$ of point $N$ can be expressed by the actual radiance $L_t$ received by sensors:

$$L_N=(L_t-L_p)\mathrm{e}^{\tau/\cos\theta_v}$$

Then:

$$E_a=\mathrm{e}^{\tau/\cos\theta_v}\sum_M \frac{L_t\cos T_N\cos T_M\,\mathrm{d}S_M}{r_{MN}^2}-L_p\mathrm{e}^{\tau/\cos\theta_v}\sum_M \frac{\cos T_N\cos T_M\,\mathrm{d}S_M}{r_{MN}^2} \tag{19}$$

After knowing the aerosol optical thickness, we can calculate adjacent terrain radiation through Eq.(18) and Eq.(19).

## 4 THE EXPERIMENTAL RESULTS AND ANALYSIS

LANDSAT-5 TM data acquainted in October 26, 2004 and 30m resolution DEM were used in the illustration. The image area locates at Miyun County, north-east suburb of Beijing, which is a part of junction area of Yanshan Mountain and the North China Plain. The area of Miyun County is 2226.5km$^2$, and the mountainous area is 1771.75km$^2$, accounting for 79.5% of the county's total area. The study area is about 256 km$^2$ vegetation covered mountain regions in Miyun County with an average altitude of 625m. The solar zenith angle and the sun azimuth of image on October 26 are 55.14° and 157.47° respectively. Continental aerosol model was chosen in this framework.

### 4.1 Experiment results

The lower surface reflectance pixels are calculated from the empirical relationship between TM7 apparent reflectance and TM band 1 and 3 land surface reflectance. After removing the pixels which are not dense vegetation area or in shaded area, we got 1356 dark pixels, accounting for 0.8918% of the whole picture. Most of these pixels were located on both sides of the ridge where the average altitude is below 800m. At that time, for the mountain peak area with the altitude above 1000m, the vegetation is sparse, the reflection is high, and the image shows bright tone.

The selected dark targets were selected to avoid the pixels lack of direct sun light, and their distribution is aggregated to some extent.

Through look-up table, the aerosol optical thickness, path

radiation and *k* value in four bands can be calculated from dark object method as shown in Table 1:

**Table 1 Parameter retrieval results**

| | TM1 | TM2 | TM3 | TM4 |
|---|---|---|---|---|
| Aerosol optical depth | 0.183 | 0.154 | 0.129 | 0.100 |
| Path radiation/($W \cdot m^{-2} \cdot sr^{-1}$) | 29.58 | 14.88 | 8.128 | 2.88 |
| *k* value | 0.2568 | 0.17189 | 0.12535 | 0.0777 |

After input the atmospheric parameters calculated from look-up table into the topographic correction algorithm, we can get the corrected results which are shown in Fig. 5.

## 4.2 Result analysis

*4.2.1 Visual comparison*

Compared with the original image, terrain effects of corrected image are basically removed. In original image, the chromatic aberration between the shaded and illuminated mountain areas is large, and the strong three-dimensional sense is obviously, besides, the phenomenon of the same object with different spectrum is obvious because of the reflectance discrepancy between shaded and illuminated mountain areas in the same terrain surface. In the corrected image, the radiance is more even, the chromatic aberration between shaded and irradiated is reduced, and three-dimensional sense is largely weakened. Due to the large zenith angle of the image, overall correction efficiency is obvious, but over-correction existed in some shaded slopes. Correction in high-brightness region is good, but not satisfactory in the areas of steep slopes and the seriously shaded areas.

*4.2.2 Comparison of histogram and statistical data*

The quality of corrected remote sensing images can be quantitatively analyzed with a variety of statistical parameters. There are so many statistical parameters which can be used to do quantitative analysis for the remote sensing images, generally, we use four parameters, maximum, minimum, mean and standard deviation to evaluate the level of information restored in the shaded regions and the spectral characteristics maintenance after the image correction. It can be seen from Table 2 that the mean of each band have a little increases and standard deviation reduces, which show that this method increase the brightness of pixels in shaded area.

Image histograms describe statistical distribution of the image pixel brightness. Fig. 6 shows the change of the image histograms before and after correction at the TM bands. Histograms of the corrected four bands look like Gaussian distribution, consistent with the random characteristics of natural features brightness, and reflect the region's statistical characteristics of the true features, and suggest the impact of the terrain effectively removal. However, the pixels in shaded slope at TM band 3 and 4 are not completely restored, and there are even a number of low brightness pixels.

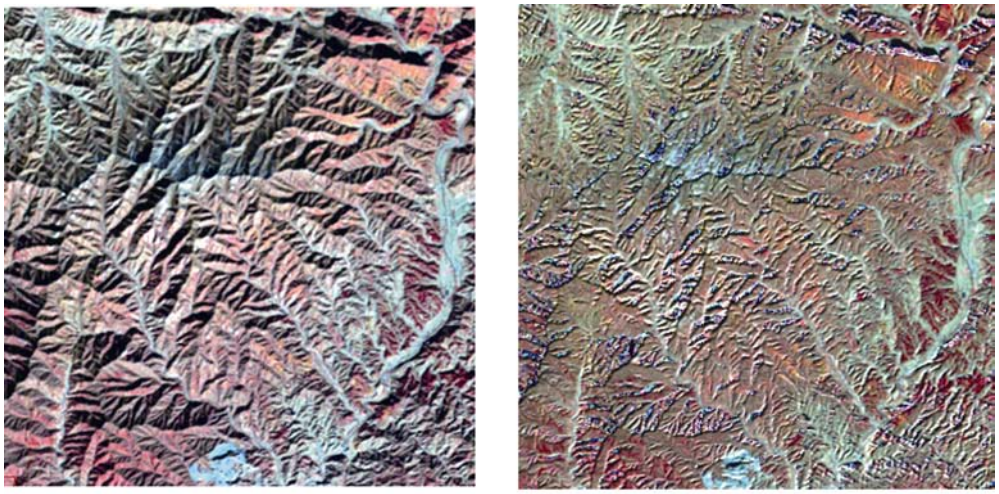


Fig. 5 Combination image of TM bands 4,3,2
(a) Original image; (b) Corrected image

**Table 2 The contrast statistic data between original and corrected image** /($W \cdot m^{-2} \cdot sr^{-1}$)

| Band | Original image | | | | Corrected image | | | |
|---|---|---|---|---|---|---|---|---|
| | Minimum | Maximum | Mean | Standard deviation | Minimum | Maximum | Mean | Standard deviation |
| 1 | 29.58 | 65.61 | 36.31 | 3.20 | 32.58 | 71.18 | 38.98 | 2.35 |
| 2 | 14.46 | 68.83 | 26.48 | 5.72 | 16.88 | 76.93 | 30.12 | 4.26 |
| 3 | 7.31 | 81.10 | 25.33 | 8.87 | 8.13 | 67.53 | 28.39 | 6.89 |
| 4 | 2.38 | 66.68 | 24.95 | 11.57 | 3.02 | 68.98 | 27.22 | 7.67 |

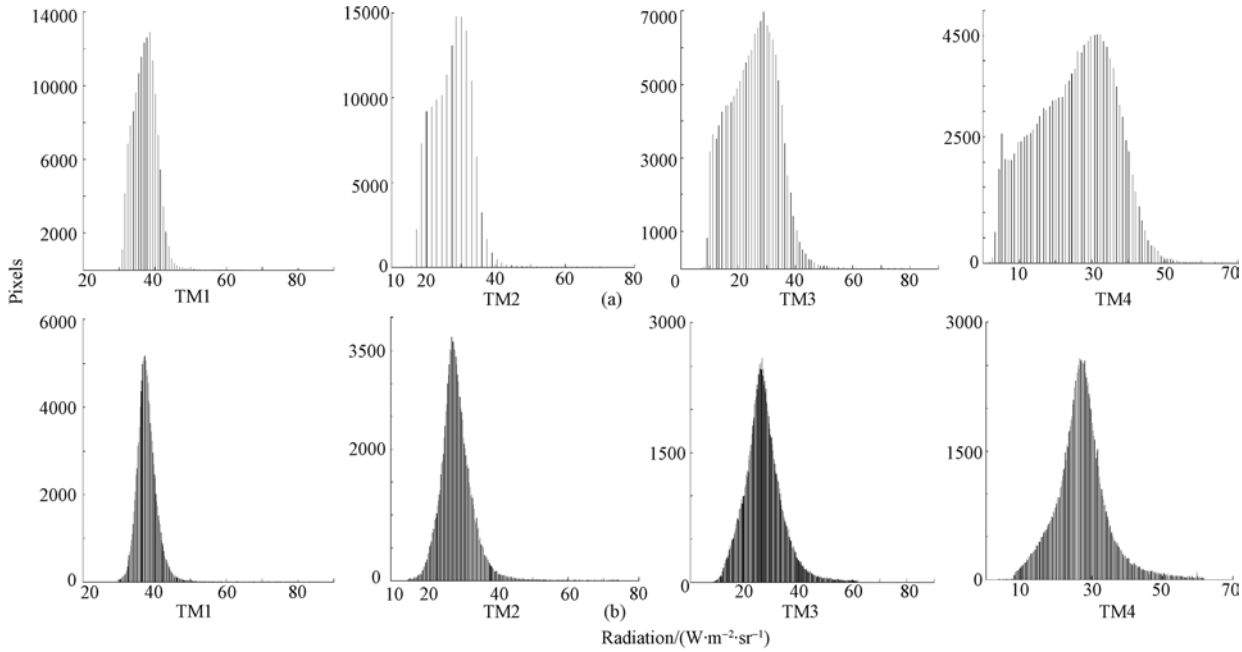


Fig. 6 The contrast of histograms between original and topographic corrected image
(a) Histograms of original images; (b) Histograms of corrected images

*4.2.3 Comparison of classified images*

Before topographic correction, radiance of sunny slopes are significantly distinct from those in shaded slopes, as a result, the classification map is significantly influenced by terrain. After topographic correction, classification results of corrected image are more consistent with the visual effects, which actually reflect the distribution of the surface. In this paper, non-supervised classification method was used to classify original and corrected images into vegetation and non-vegetation as what are shown in Fig. 7.

Firstly, we select vegetation and non-vegetation areas in the shaded areas and sunny areas from the image, and classify them into four categories: shaded vegetation, sunlit vegetation, shaded non-vegetation and sunlit non-vegetation, then we calculate radiance change in each category of different features at each band before and after correction, which are shown in Table 3. From the table, we can see that compared with the original image, the average radiance of the corrected shaded pixels increases, while the average radiance of the sunny radiance pixels decreases, and the same class tend to have the similar radiance.

Table 4 shows the spectrums before and after correction in vegetation and non-vegetation region, when select a variety of light factor (cosi). After the correction, the spectral values of vegetation and non-vegetation areas may increase or decrease, but the radiance are more similar compared to the original image, which proves the method is effective for the mountain terrain correction. In vegetation area, radiance in regions with smaller light factors increase after correction, while in regions

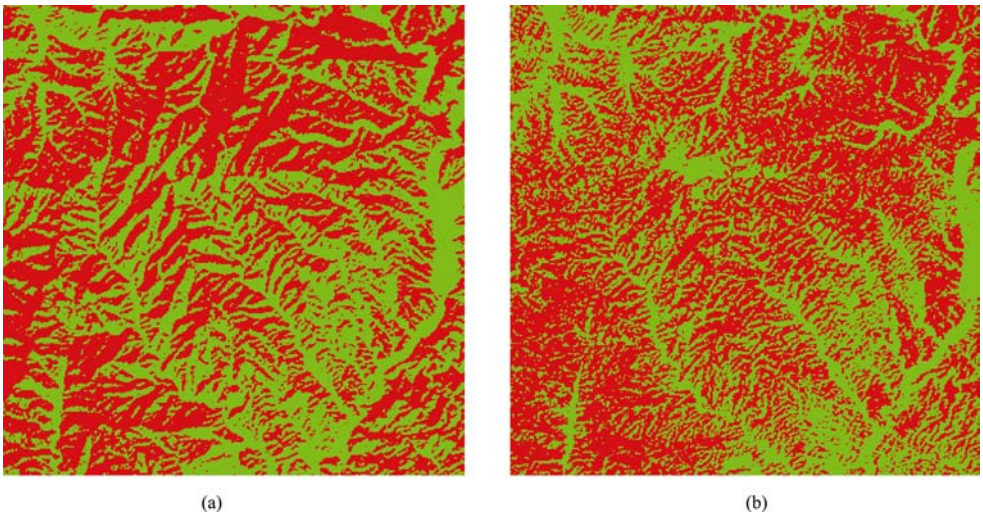


Fig. 7 Results of unsupervised classification
(a) Original image classification; (b) Corrected image classification
(Red areas mean vegetation, green areas mean non-vegetation)

**Table 3 The contrast of average radiances of vegetation and non-vegetation area between original and topographic corrected images** /(W·m$^{-2}$·sr$^{-1}$)

| Band | Vegetation | | | | Non-vegetation | | | |
|---|---|---|---|---|---|---|---|---|
| | Pre-corrected | | Corrected | | Pre-corrected | | Corrected | |
| | Sunny | Shaded | Sunny | Shaded | Sunny | Shaded | Sunny | Shaded |
| 1 | 38.26 | 33.58 | 36.23 | 38.92 | 38.45 | 32.96 | 36.72 | 37.21 |
| 2 | 30.32 | 20.85 | 25.92 | 27.24 | 32.17 | 18.12 | 26.33 | 28.34 |
| 3 | 29.15 | 14.61 | 22.12 | 24.78 | 31.28 | 11.61 | 23.97 | 23.36 |
| 4 | 38.02 | 9.02 | 25.98 | 27.23 | 38.59 | 7.12 | 25.47 | 22.56 |

**Table 4 The contrast of average radiances of vegetation and non-vegetation area between original and topographic corrected images in characteristic light factors** /( W·m$^{-2}$·sr$^{-1}$)

| Band | | 1 | | 2 | | 3 | | 4 | |
|---|---|---|---|---|---|---|---|---|---|
| Cosi | | Pre-corrected | Corrected | Pre-corrected | Corrected | Pre-corrected | Corrected | Pre-corrected | Corrected |
| Vegetation | 0.1 | 33.93 | 36.06 | 19.31 | 26.12 | 12.67 | 23.81 | 8.54 | 22.70 |
| | 0.5 | 35.01 | 36.63 | 25.82 | 26.80 | 23.89 | 24.72 | 23.77 | 24.59 |
| | 0.9 | 38.25 | 36.17 | 31.19 | 26.09 | 31.96 | 24.81 | 38.04 | 26.11 |
| Non-Vegetation | 0.1 | 34.66 | 41.97 | 22.03 | 35.81 | 16.76 | 35.55 | 12.22 | 33.71 |
| | 0.5 | 39.28 | 39.49 | 30.51 | 31.44 | 30.69 | 31.65 | 28.11 | 30.87 |
| | 0.9 | 43.24 | 40.61 | 36.2 | 32.93 | 31.8 | 30.19 | 40.22 | 29.11 |

with larger light factors, radiance decrease after correction. TM Bands 1—3 have better correction results, and the radiance are more consistent after correction; while for TM band 4, a certain degree of under correction exist in vegetation region lacking of sun light where the light factors are comparatively low. However, in non-vegetation areas, spectral values increase significantly in lower light factor areas after correction, these pixels located in shaded face, where over correction is obvious. The reason for the over correction and under correction are: the precision or registration accuracy of corresponding region digital elevation model is not high, as well as the atmospheric parameters errors caused by retrieval.

*4.2.4 Error Estimation*

Because of the complex mechanism and the assumptions of physical models, the errors are inevitable. In this paper, aerosol optical thickness is derived from dark object method. Iqnatov discussed potential error when extracting aerosol optical thickness from dark object (Vermote *et al.*, 1997). In theory, when the optical thickness is smaller, the error was from 5% to 10%. For the situation with large optical thickness, the error can be as high as 20%. In this paper, the study area has clean atmosphere and a smaller optical thickness. The error of the aerosol optical thickness retrieval was assumed to be 8%. The ranges of optical thickness are listed in Table 5.

Choose the first band to do further error analysis, take the scope of aerosol optical thicknesses into 6S, parameters of TM1 are as follows:

**Table 5 The range of aerosol optical thickness**

| | TM1 | TM2 | TM3 | TM4 |
|---|---|---|---|---|
| The range of aerosol optical thickness | 0.16836—0.19764 | 0.14168—0.16632 | 0.11868—0.13932 | 0.092—0.108 |

**Table 6 The area of TM1 image parameters**

| | The average | The lowest | The highest |
|---|---|---|---|
| Aerosol Optical Depth | 0.183 | 0.16836 | 0.19764 |
| Path radiation/(W·m$^{-2}$·sr$^{-1}$) | 29.58 | 29.021 | 30.135 |
| *k* value | 0.2568 | 0.2753 | 0.2381 |

Taking the parameters into the topographic correction model, we can get the range how much the dark object method impacts the results of corrected image radiance. The mean of the corrected radiance of TM band 1 image is 38.98 W·m$^{-2}$·sr$^{-1}$, and the range of mean value caused by error is 38.56—39.43 W·m$^{-2}$·sr$^{-1}$(Table 6).

## 5 CONCLUSIONS

This paper proposes a specific method to correct topographic effects. The new correction model is based on the radiation transfer equation and is more reliable compared with empirical models. Besides, through reasonable approximations and equation simplification, the disadvantages of conventional physical model equations are avoided, such as high complexity of the equations, a large number of input parameters, and so on.

From analysis of the statistics properties, histograms and classification data of the corrected images, we can find that the new method effectively corrects radiance of satellite remote sensing data, and eliminate the terrain effects, which is consistent to the judging from visual interpretation. This method does not require simultaneous measurements of atmospheric parameters. Just by introducing the ratio of diffuse scattering radiance to the direct sun radiance, the correction model reduces

the amount of required parameters, which need to be retrieved from the image. It is helpful to solve the underdetermined problem of topographic correction. At the same time, it also improves the reliability of topographic correction, and makes it convenient for further process of remote sensing images in mountain areas.

## REFERENCES


Collins J B and Woodcock C E. 1996. An assessment of several linear change detection techniques for mapping forest mortality using multi-temporal Landsat TM data. *Remote Sens. Environ*, **56**: 66—77

Dozier J and Frew J. 1990. Rapid calculation of terrain parameters for radiation modeling from digital elevation data. *IEEE Trans. Geosci. Remote Sens*, **28**: 963—969

Franklin J, Logan T L, Woodcock C E and Strahler A H. 1986. Coniferous forest classification and inventory using Landsat and digital terrain data. *IEEE Trans. Geosci. Remote Sens*, **24**(1): 139—149

Hill J and Sturm B. 1991. Radiometric. correction of multi-temporal thematic mapper data for use in agricultural land-cover classification and vegetation monitoring. *Int. J. Remote Sens*, **12**: 1471—1491

Itten K I and Meyer P. 1993. Geometric and radiometric correction of TM data of mountainous forested areas. *IEEE Trans. Geosci. Remote Sensing*, **31**: 764—770

King M D, Kaufman Y J, Tanre D and Nakajima T. 1999. Remote sensing of tropospheric aerosols from spcace: past, present, and future. *Bulletin of the American Meteorological Society*, **80**: 2229—2259

Olsson H. 1995. Reflectance calibration of thematic mapper data for forest change detection. *Int. J. Remote Sensing*, **16**: 81—96

Proy C, Tanre D and Deschampls P Y. 1989. Evaluation of topographic effects in remotely sensed data. *Remote Sens. Environ*, **30**: 21—32

Remer L A, Kaufman Y J, Tanre D and Matto S. 2005. The MODIS aerosol algorithm, products, and validation. *Journal of the Atmospheric Sciences*, **62**(4): 947—927

Richter R. 1996a. A spatially adaptive fast atmospheric correction algorithm. *International Journal of Remote Sensing*, **17**: 1201—1214

Richter R. 1996b. Atmospheric correction of satellite data with haze removal including a haze/clear transition region. *Computers & Geosciences*, **22**: 675—681

Schaaf C B, Li X and Strahler A H. 1994. Topographic effects on bidirectional and hemispherical reflectances calculated with a geometric-optical canopy model. *IEEE Trans.Geosci. Remote Sensing*, **32**: 1186—1193

Vermote E F, Tanre D J, Deuze L, Herman and Morcrette J. 1997. Second simulation of the satellite signal in the solar spectrum, 6S: an overview. *IEEE Trans. Geosci. Remote Sens*, **35**: 675—686

Wang X Q, Yang S Z, Zhu Y H and Yi W N. 2003. Aerosol optical thickness retrieval over land from MODIS data based on the inversion of the 6S model. *Chinese Journal of Quantum Electronics*, **20**(5): 629—634

Yan G J, Zhu C G, Guo J, Wang J D and Li X W. 2000. A model based radiative transfer algorithm to correct remotely sensed image in mountainous area. *Journal of Image and Graphics*, (1): 11—15

Zhao C J, Song X Y, Wang J H, Liu L Y and Li C J. 2007. An algorithm based on 6S model for removing atmospheric effects form satellite imagery pixel by pixel. *Optical Technique*, **33**(1): 11—15

Zheng W and Zeng Z Y. 2004. A review on methods of atmospheric correction for remote sensing images. *Remote Sensing Information*, **4**: 66—67

Zhong Y W, Liu L Y, Wang J H and Yan G J. 2006. A method based on moment matching algorithm to correct remotely sensed image in rugged area. *Geography and Geo - Information Science*, **1**: 31—34

# 光学遥感影像表观辐亮度地形效应纠正物理模型

史　迪, 阎广建, 穆西晗

北京师范大学 地理学与遥感科学学院 遥感科学国家重点实验室, 北京　100875

摘　要: 针对已有地形纠正方法的不足, 在山区辐射传输模型简化的基础上, 提出了水平地面上接收到的漫射辐射与垂直于太阳方向表面接收的直射辐射比例因子的概念, 建立了仅需要太阳角度信息和大气模式作为输入参数, 主要针对地形效应本身进行纠正的简单纠正模型, 可以将复杂地形区光学遥感影像表观辐亮度纠正为无地形影响的水平地表辐亮度, 并以 TM 影像为例进行了实验验证。

关键词: 地形纠正, 表观辐亮度, 物理模型, 气溶胶光学厚度, 6S

中图分类号: TP701　　文献标识码: A

## 1 引　言

遥感图像在广泛地运用于各行各业定量分析之前, 首先要对其进行辐射纠正, 包括系统辐射定标、大气效应纠正、太阳入射角纠正和地形效应纠正等, 其中地形纠正最为复杂。地形效应不仅会产生同物异谱或同谱异物现象, 即相同地物具有不同辐射亮度或不同地物辐射亮度近似, 还会造成像元尺度上“各向异性反射”现象(Schaaf, 1994)。从而对遥感数据进一步在土地分类、资源管理, 特别是山区森林资源监测产生不利的影响(Collins & Woodcock, 1996; Olsson, 1995; Itten & Meyer, 1993)。中国山地占各类地形的 33%, 因此地形辐射纠正对遥感应用尤为重要。

遥感图像地形纠正的方法很多, 主要分为经验模型和物理模型 2 种。经验模型简便、实用, 包括波段比模型、主成分分析模型以及回归分析模型等。它们的理论依据是对一系列遥感参数作经验性的统计分析, 建立遥感参数与地面观测数据之间的回归方程。这类模型对研究区域有很强的依赖性, 在不同区域需要建立不同的模型, 且模型和参数没有明确的物理意义。物理模型是基于对辐射源定量物理分析, 建立描述辐射和地表相互作用物理过程的辐射传输方程进行地形辐射纠正, 如阎广建等(2000)的基于光源分析的模型。模型中的辐射源一般包括太阳直射辐射、天空漫散射和邻近地形的反射辐射 3 部分。物理模型中的参数具有明确的物理意义, 适用更广泛, 在一定程度上避免了经验模型的景观依赖。但是物理模型的缺点在于: 方程复杂、输入参数多, 给研究工作带来困难, 因此为了求解通常对多个非主要因素进行忽略或假定。

本文的研究目的在于探索一种简便的能去除地形效应的纠正方法。该方法基于山区辐射传输模型, 考虑大气吸收透过率和大气与地表间多次反射作用, 建立了山地到平地的像元辐亮度转换公式。通过模型简化, 实现仅用少量输入参数即能对遥感卫星图像实现较为精确的地形纠正的方法。实验选择了北京密云县的一块研究区域, 采用了 Landsat-5 TM 卫星影像和对应的 DEM, 并对结果进行分析, 发现新地形纠正方法有效地去除了地形差异。

## 2 地形纠正模型的建立

### 2.1 山地辐射传输方程

山地辐射与地表相互作用机理复杂, 方程求解困难。很多研究假设地表为朗伯体(阎广建等, 2000; Franklin 等, 1986; Hill & Radiometric, 1998; Richter, 1996a,1996b)以及大气散射为各向同性。对于朗伯地表, 传感器接收到的辐亮度 $L$ 包括经大气衰减后的地表反射辐射和大气自身反射(也即程辐射)2 部分,

收稿日期: 2008-05-09; 修订日期: 2009-01-07

基金项目: 国家自然科学基金项目(编号: 40871164)、国家 973 项目(编号: 2007CB714402)和欧盟 FP7 计划(编号: 212921)联合资助。

第一作者简介: 史迪(1983— ), 女, 四川成都人, 研究生, 从事光学遥感领域的研究。

通讯作者: 阎广建 gjyan@bnu.edu.cn

表示为:

$$L = L'\mathrm{e}^{-\tau/\cos\theta_\mathrm{v}} + L_\mathrm{p} \tag{1}$$

式中, $\theta_\mathrm{v}$ 为观测天顶角, $\tau$为大气总光学厚度, $L_\mathrm{p}$ 为传感器上所接收的程辐射, $L'$为地表反射辐亮度。

地表一点反射辐亮度来源于地表接收的 3 部分有效光照 $E$ (钟耀武等, 2006): 太阳的直接入射辐射照度 $E_\mathrm{d}$; 天空漫散射照度 $E_\mathrm{f}$; 周围地形的反射辐射 $E_\mathrm{a}$。设在观测方向地表的反射率为$\rho$, 则任意一像元所反射的总的辐射亮度可表示为 $L'$:

$$L' = \rho\left(E_\mathrm{d} + E_\mathrm{f} + E_\mathrm{a}\right)/\pi = \rho E/\pi \tag{2}$$

### 2.2 辐照度的计算方法

#### 2.2.1 直射光辐照度

太阳辐射穿过大气层直接到达地球表面, 单位面积上入射能量既和辐射与地表所成几何关系密切相关, 又是大气光学厚度的函数。假设大气层由若干水平均匀的薄层构成, 则入射到坡面的直接辐射 $E_\mathrm{d}$ 可表示为:

$$E_\mathrm{d} = \Theta\cos i E_0\mathrm{e}^{-\tau/\cos\theta_\mathrm{s}} \tag{3}$$

式中, $\Theta$为地形遮蔽系数, 若坡面为阴影区, $\Theta$为 0, 否则为 1; $E_0$为大气层顶部垂直于太阳入射方向所接收的辐照度; $\tau$ 为总的垂直大气光学厚度; $\theta_\mathrm{s}$为太阳天顶角。式中, 太阳有效入射角 $i$ 定义为: 太阳入射光线和被照坡面法线的夹角, 计算公式如下:

$$\cos i = \cos\theta_\mathrm{s}\cos\theta_\mathrm{p} + \sin\theta_\mathrm{p}\sin\theta_\mathrm{s}\cos\left(\phi - A\right) \tag{4}$$

式中, $\phi$为太阳方位角; $\theta_\mathrm{p}$为坡面的坡度; $A$ 为坡面的坡向。

#### 2.2.2 天空漫散射辐照度

太阳辐射通过大气遇到空气分子、尘粒、云滴等质点时, 辐射方向改变, 使太阳辐射以质点为中心向四面八方传播开来形成天空漫散射。漫散射与引起散射的各种粒子的特性、太阳入射角度有关, 呈各向异性分布。本文中忽略各向异性的复杂性, 假设天空漫散射各向同性分布, 引入天空观测因子 $V$, 表示坡面一点所接收的天空漫散射与未被遮挡的水平表面所接收的漫散射 $E_\mathrm{f}^\mathrm{h}$ 之比(Dozier & Frew, 1990)。

$$E_\mathrm{f} = VE_\mathrm{f}^\mathrm{h}$$

$$V \approx \frac{1}{2\pi}\int_0^{2\pi}[\cos\theta_\mathrm{p}\sin^2 H_\phi + \sin\theta_\mathrm{p}\cos(\phi - A)(H_\phi - \sin H_\phi\cos H_\phi)]\mathrm{d}\phi \tag{5}$$

式中: $H_\phi$为在$\phi$方向的最大天空张角。

#### 2.2.3 周围地形反射辐照度

忽略大气吸收对周围地形反射辐射的影响, 基于 Proy 等(1989)的分析, 假设像元为朗伯体, 采用逐点计算的方式, 周围各点 $M$ 对一点 $N$ 的反射辐射可表示为 $E_\mathrm{a}\,(\mathrm{W\cdot m^{-2}})$:

$$E_\mathrm{a} = \sum_M \frac{L_M\cos T_N\cos T_M\mathrm{d}S_M}{r_{MN}^2} \tag{6}$$

式中, $L_M$ 表示点 $M$ 的亮度; $T_M$ 及 $T_N$分别表示点 $M$ 及点 $N$坡面法线与 $MN$ 连线的夹角; $\mathrm{d}S_M$为像元 $M$ 的实际面积; $r_{MN}$为点 $M$ 和 $N$ 间的距离(图 1)。

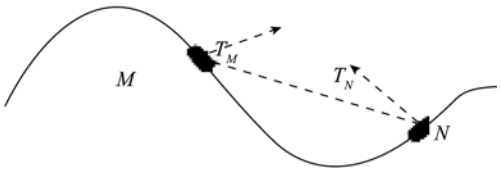


图 1 两个邻近像元点的位置关系

### 2.3 地形纠正模型建立

6S (Second Simulation of the Satellite Signal in the Solar Spectrum)模型是 20 世纪 90 年代中后期 Vermote 等(1997)在 5S 模型上发展起来的, 包括大陆型、海洋型、城市型、背景沙漠型、用户自定义型等多种大气气溶胶模型, 还提供了中纬度夏季、中纬度冬季、美国标准大气、热带大气、亚北极、亚南极型等 6 种大气模式, 以及 9 种二向性反射模型, 是目前较为成熟的大气纠正模型之一。仿照 6S, 定义大气对直射光的上下行吸收透过率为 $T(\theta_\mathrm{s},\ \theta_\mathrm{v})$, 太阳下行辐射的漫射透过率为 $t_\mathrm{d}(\theta_\mathrm{s})$, 地表反射的上行辐射的漫射透过率为 $t_\mathrm{d}(\theta_v)$。考虑大气与地表的多次散射, 得到某像元的表观辐亮度为:

$$L = T\left(\theta_\mathrm{s},\theta_\mathrm{v}\right)\left\{\frac{E}{\pi\left(1-\bar{\rho}S\right)}\left[\mathrm{e}^{-\tau/\cos\theta_\mathrm{v}}\rho + \bar{\rho}t_\mathrm{d}\left(\theta_\mathrm{v}\right)\right] + L_\mathrm{P}\right\} \tag{7}$$

式中, $S$ 为大气球形反照率, $\bar{\rho}$ 为下垫面平均反射率, $\rho$为像元反射率。定义水平地面接收到的天空漫散射为 $E_\mathrm{f}^\mathrm{H}$, 与太阳入射方向垂直的表面所接收的直射辐射为 $E_i$, 则水平地面接收到的直射辐射为

$$E_i^\mathrm{h} = E_i\cos\theta_\mathrm{s} = E_0\cos\theta_\mathrm{s}\mathrm{e}^{-\tau/\cos\theta_\mathrm{s}}\ 。$$

依据 6S 中关于漫射透过率和直射透过率的定义有:

$$t_\mathrm{d}\left(\theta_\mathrm{s}\right)\big/\mathrm{e}^{-\tau/\cos\theta_\mathrm{s}} = E_\mathrm{f}^\mathrm{h}\big/E_i^\mathrm{h} = E_\mathrm{f}^\mathrm{h}\big/E_0\cos\theta_\mathrm{s}\,\mathrm{e}^{-\tau/\cos\theta_\mathrm{s}} \tag{8}$$

定义水平地表漫射辐射和与太阳方向垂直表面的直射辐射比例因子 $k$, 即 $E_\mathrm{f}^\mathrm{h}/E_i = k$, 则有:

$$t_\mathrm{d}\left(\theta_\mathrm{s}\right)/\mathrm{e}^{-\tau/\cos\theta_\mathrm{s}} = k/\cos\theta_\mathrm{s} \tag{9}$$

这个关系虽然是基于水平地表接收天空散射和太阳直射辐射的比例建立的, 但是对于观测方向, 也可用来描述散射透过率和直射透过率的比率。从

后文的分析可以发现，这个 $\boldsymbol{k}$ 是仅随太阳光入射天顶角的余弦和气溶胶光学厚度单调变化的，即通过太阳入射天顶角的余弦和气溶胶光学厚度可求解唯一的 $\boldsymbol{k}$。这对于山地辐射方程的简化以至大气效应纠正是有利的。

任一像元卫星接收到的辐射亮度为:

$$L = T(\theta_s,\theta_v)\left\{E_i\frac{\Theta\cos i + Vk + E_a/E_i}{\pi(1-\bar{\rho}S)}\times [e^{-\tau/\cos\theta_v}\rho + e^{-\tau/\cos\theta_v}\bar{\rho}k/\cos\theta_v] + L_p\right\} \quad (10)$$

相同像元，假设地表为平地，没有周围环境的反射，天空光也没有被遮挡，表观辐射亮度为:

$$L_x = T(\theta_s,\theta_v)\left\{E_i\frac{\cos\theta_s + k}{\pi(1-\bar{\bar{\rho}}S)}[e^{-\tau/\cos\theta_v}\rho + e^{-\tau/\cos\theta_v}\bar{\bar{\rho}}k/\cos\theta_v] + L_p\right\} \quad (11)$$

TM 等中高分辨率卫星传感器近似垂直观测，视场角窄，将观测角度设为 0°，忽略$\rho$，$\bar{\rho}$，$\bar{\bar{\rho}}$ 差异得到仅用来纠正地形效应的纠正模型:

$$L_x = \frac{[L - T(\theta_s,0°)L_p][\cos\theta_s + k]}{\Theta\cos i + Vk + E_a/E_i} + T(\theta_s,0°)L_p \quad (12)$$

## 3　参数的反演与计算

从原始图像和 DEM 可以得到太阳天顶角、方位角以及各像元点的坡度、坡向等各种地形因子。由公式(12)可见，完成地形纠正仍需要从图像或其他辅助数据中得到 $T(\theta_s,0°)L_p$、$k$ 和 $E_a/E_i$ 3 个参数。本文假设观测天顶角为 0°，以 Landsat-5 TM 卫星影像数据为例进行地形纠正。对于其他垂直观测窄视场中高分辨率遥感图像的地形纠正，所提出的方法同样适用。本文参数反演的主要方法是针对不同大气模式，利用 6S 提供的大气参数，建立不同大气状况下的 2 类查找表，插值计算出所需参数。

### 3.1　大气参数查找表的建立

经分析在大气模式和气溶胶模式固定情况下，模型中需要的大气参数 $k$ 和 $T(\theta_s,0°)L_p$ 仅随太阳天顶角和气溶胶光学厚度变化。更进一步，不同大气模式下 $k$ 和 $T(\theta_s,0°)L_p$ 的关系有微小的差异，所以在某一种大气模式下建立的关系具有一定的普适性。图 2 为大陆型气溶胶模式下 TM1 波段 $T(\theta_s,0°)L_p$ 和 $k$ 随太阳天顶角和气溶胶光学厚度变化趋势。本文利用 6S 建立了不同气溶胶模式下气溶胶光学厚度、太阳天顶角与大气参数 $T(\theta_s,0°)L_p$ 和 $k$ 的查找表(查找表 1)。每种气溶胶模式下建立的查找表包括 6 个气溶胶光学厚度(0.05, 0.1, 0.3, 0.5, 0.7, 1)，6 个太阳天顶角(0.71°, 16.19°, 38.45°, 46.19°, 59.81°, 67.5°)。在知道气溶胶模式、气溶胶光学厚度和太阳天顶角后，就可以利用该查找表得到所关心的大气参数。其中气溶胶光学厚度结合暗目标法求得，具体方法将在 3.2 节阐述。

### 3.2　气溶胶光学厚度反演

目前从遥感影像中获取气溶胶光学厚度的方法有分类匹配法、对比估计法和暗目标法等(郑伟 & 曾志远, 2004; 王新强等, 2003; 赵春江等, 2007)。Kaufman 和 Tanre 提出的暗目标法是目前陆地上空反演气溶胶光学厚度应用最广泛的方法，在海洋、浓密植被以及内陆水体区域取得了很好的效果(King 等, 1999; Remer 等, 2005)。其原理是利用 2.13μm (TM7 波段)具有对尘土外其他气溶胶粒子透明，从而不考虑气溶胶散射的特点，只要消除水汽

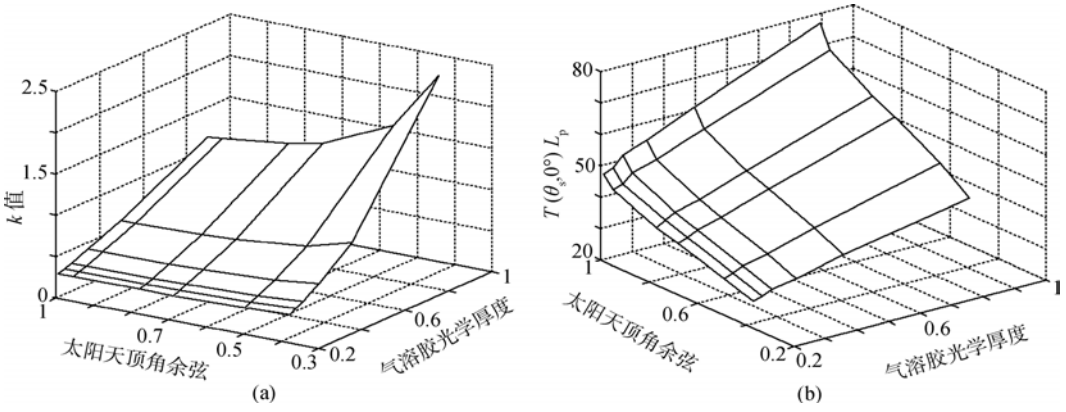


图 2　大陆模式中纬度冬季 TM1 波段 $T(\theta_s, 0°)L_p$ 和 $k$ 变化趋势图

(a) $k$ 值与太阳天顶角余弦和气溶胶光学厚度关系; (b) $T(\theta_s, 0°)L_p$ 与太阳天顶角余弦和气溶胶光学厚度关系

的吸收就可以认为地表反射率就是表观反射率。并且暗目标在 2.13μm(TM7 波段)处反射率与 0.4—0.48μm(TM1 波段)处反射率和 0.6—0.68μm(TM3 波段)处反射率有固定的经验关系。获取 TM1、TM3 的地表反射率后，由于暗目标的表观反射率已求出，通过对 TM1、TM3 波段的查找表进行插值运算就可以确定气溶胶光学厚度。

反演过程依据 Kaufman 和 Tanre 的方法对暗目标像元一个个的反演。首先根据对暗目标$\rho_1$=0.01, $\rho_3$=0.02 的假设，反推出 TM7 波段植被反射率在 0.036—0.044 范围的暗像元。然后联合地形因子去除处于阴影区的像元。最后利用归一化差分植被指数(NDVI)判断是否为浓密植被。依据地表反射率在 TM1、TM3 和 TM7 波段的经验关系，即$\rho_1=\rho_7'/4$, $\rho_3=\rho_7'/2$，求出暗目标在 TM1、TM3 波段的地表真实反射率。结合这 2 个波段的表观反射率，利用查找表 2 得到对应波段的气溶胶光学厚度。

查找表 2 是根据太阳天顶角、地表反射率、表观反射率和气溶胶光学厚度的关系，查找得到气溶胶光学厚度。查找表建立时依据暗目标反射率的范围，选取 5 个地面反射率(0.005, 0.01, 0.05, 0.2, 0.5), 5 个表观反射率(0.005, 0.01, 0.05, 0.2, 0.5), 6 个太阳天顶角(0.71, 16.19, 38.45, 46.19, 59.81, 67.5)，通过 6S 计算得到对应的 TM1 和 TM3 波段气溶胶光学厚度。利用查找表求取 TM1 和 TM3 波段气溶胶光学厚度时，其他输入参数在它们之间进行线性内插。对于其他波段的气溶胶光学厚度，可以根据以下公式进行计算(Remer 等, 2005):

$$\tau_i = a\,\lambda_i^{-b} \tag{13}$$

式中，$\tau_i$ 是该波段的气溶胶光学厚度；$\lambda_i$ 是对应波段的中心波长；$a$ 和 $b$ 分别称为埃系数，通过逐个像元回归取得。

在反演气溶胶光学厚度时，暗像元在 TM7 波段的表观反射率 $\rho_Q'$ 为:

$$\rho_Q' = \frac{\pi L_Q d^2}{E_0 \cos\theta_s} \tag{14}$$

式中, $L_Q$ 是 $Q$ 像元的表观辐射亮度, $d$ 是天文单位的日地距离，典型日期的日地距离。

### 3.3　求取瑞利散射光学厚度

瑞利散射光学厚度在不同气溶胶模式下仅有微小变化，可近似用相同数值表示，此外仅随像元高度变化。运行 6S 求每个波段 0, 1, 2.5km 高度下瑞利散射光学厚度，分别作出 TM 四个波段的瑞利散射光学厚度与高度的函数关系。如图 3 所示，每个波段的瑞利散射光学厚度与高度有如下函数关系，$\tau_{\text{raleigh}}1$，$\tau_{\text{raleigh}}2$, $\tau_{\text{raleigh}}3$, $\tau_{\text{raleigh}}4$ 是 4 个波段的瑞利散射光学厚度, $h$ 是目标地物高度:

$$\begin{aligned}
\tau_{\text{rayleigh}}1 &= -0.017h + 0.165\\
\tau_{\text{rayleigh}}2 &= -0.008h + 0.085\\
\tau_{\text{rayleigh}}3 &= -0.004h + 0.046\\
\tau_{\text{rayleigh}}4 &= -0.001h + 0.017
\end{aligned} \tag{15}$$

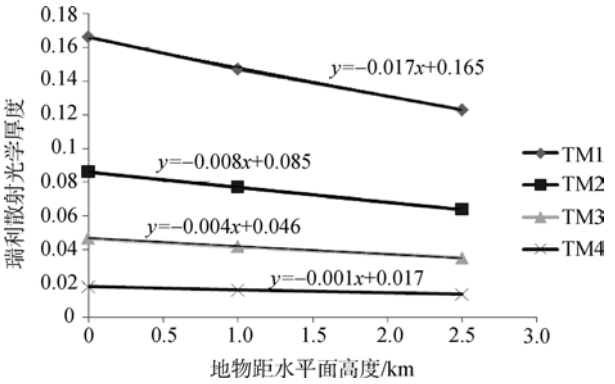


图 3　瑞利散射光学厚度与目标物水平高度关系

计算大气总光学厚度可由以下公式得到:

$$\tau = \tau_{\text{rayleigh}} + \tau_{\text{aerosols}} \tag{16}$$

式中：大气总光学厚度为 $\tau$，气溶胶光学厚度为 $\tau_{\text{aerosols}}$，瑞利散射光学厚度为 $\tau_{\text{rayleigh}}$。

### 3.4　求取气体总吸收透过率

大气的吸收透过率随太阳天顶角和目标像元的水平面高度变化。高度变化对总大气吸收透过率的影响在 TM1、TM2、TM3 波段非常小，对 TM4 波段高程 2.5km 内最大有 6.1%的影响。因此在海拔高度变化低于 3km 的山区，计算气体总吸收透过率时可近似认为吸收透过率不受高程变化而变化。取海平面高度和 2.5km 不同太阳天顶角下的气体总吸收透过率的平均值作为近似值，分别做出 TM 4 个波段的气体总吸收透过率与太阳天顶角余弦的函数关系。如图 4，每个波段的气体总吸收透过率与太阳天顶角余弦有如下函数关系:

$$\begin{aligned}
T_{g1} &= -0.152\cos\theta_s^2 + 0.247\cos\theta_s + 0.886\\
T_{g2} &= -0.59\cos\theta_s^2 + 0.974\cos\theta_s + 0.527\\
T_{g3} &= -0.411\cos\theta_s^2 + 0.677\cos\theta_s + 0.668\\
T_{g4} &= -0.065\cos\theta_s^2 + 0.139\cos\theta_s + 0.894
\end{aligned} \tag{17}$$

$T_{g1}$，$T_{g2}$，$T_{g3}$，$T_{g4}$ 是 4 个波段的气体总吸收透过率, $\cos\theta_s$ 是太阳天顶角余弦。

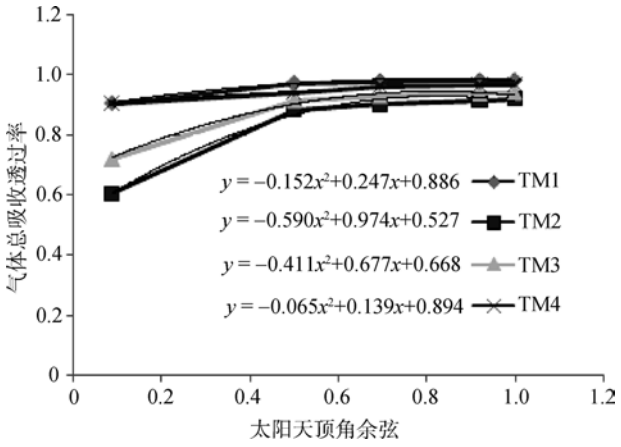


图 4　气体总吸收透过率与太阳天顶角余弦关系

### 3.5　计算环境辐射

由公式(6)可得:

$$\frac{E_a}{E_i}=\sum_M \frac{L_M \cos T_N \cos T_M \mathrm{d}S_M}{r_{MN}^2 E_i} \tag{18}$$

可见，要计算周围环境辐射项 $E_a/E_i$，首先要知道周围各像元点的亮度。为了解决这种自相矛盾的问题，我们假设传感器接收到的辐射可被方程(1)精确表征。则 $N$ 点的辐射亮度 $L_N$ 可用传感器接收到的实际辐射亮度 $L_t$ 表示为:

$$L_N=(L_t-L_p)\mathrm{e}^{\tau/\cos\theta_\mathrm{v}}$$

则有:

$$E_\mathrm{a}=\mathrm{e}^{\tau/\cos\theta_\mathrm{v}}\sum_M \frac{L_t \cos T_N \cos T_M \mathrm{d}S_M}{r_{MN}^2}-$$
$$L_P\mathrm{e}^{\tau/\cos\theta_\mathrm{v}}\sum_M \frac{\cos T_N \cos T_M \mathrm{d}S_M}{r_{MN}^2} \tag{19}$$

在知道了气溶胶光学厚度之后，通过公式(18)、(19)就可以得到周围环境辐射项。

## 4　实验结果与分析

实验采用的数据是 2004-10-26 获取的 Landsat-5 TM 卫星影像以及对应的 30m×30m 分辨率 DEM。图像所在区域是北京东北部郊区密云县，属燕山山地与华北平原交接地。密云全县面积 2226.5km$^2$，其中山区面积 1771.75km$^2$，占全县总面积的 79.5%。研究区域选择北京密云县面积 256km$^2$ 的山地，区域为植被覆盖的山地，平均海拔高度 625m。2004-10-26 影像成像时太阳天顶角为 55.14°，太阳方位角 157.47°。研究区域选取大陆型气溶胶模式。

### 4.1　实验结果

由 TM7 表观反射率与 TM1 和 TM3 波段地表反射率的经验关系计算出地表反射率较低的像元，去除非浓密植被和被遮蔽像元，得到暗像元 1356 个，占全图总像元数的 0.8918%，大多分布在平均海拔高度 800m 以下的山脊两侧。此时海拔 1000m 以上山顶植被稀少，反射率较高，呈明亮色调。选取的暗目标很好地避免了未受直接光照的像元，分布有一定聚集性。

通过查找表计算，由暗目标法反演得到各波段气溶胶光学厚度、程辐射和 $k$ 值如表 1。

将通过查找表得到的大气参数带入地形纠正公式，得到纠正结果见图 5。

**表 1**　参数反演结果

| | TM1 | TM2 | TM3 | TM4 |
|---|---|---|---|---|
| 气溶胶光学厚度 | 0.183 | 0.154 | 0.129 | 0.100 |
| 程辐射/(W·m$^{-2}$·sr$^{-1}$) | 29.58 | 14.88 | 8.128 | 2.88 |
| $k$ 值 | 0.2568 | 0.17189 | 0.12535 | 0.0777 |

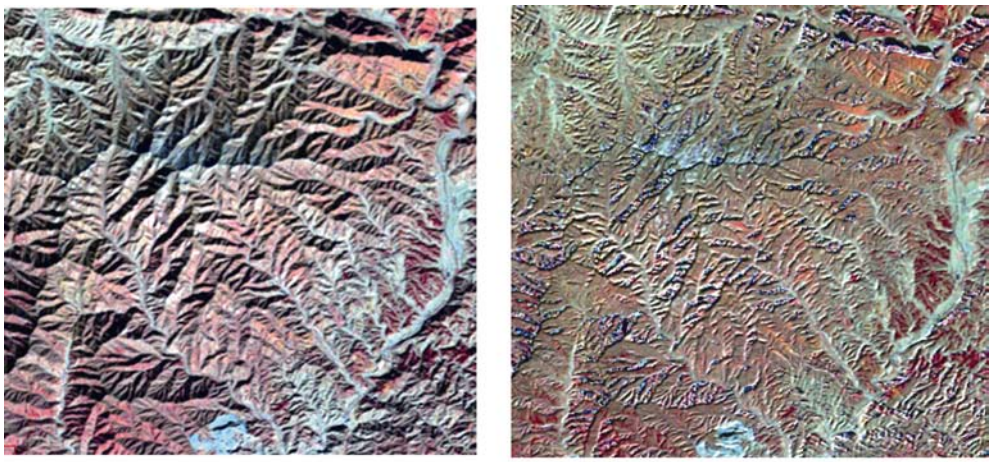

(a)　(b)

图 5　TM 4、3、2 波段假彩色合成图像

(a)原始图像; (b)经过纠正的图像

### 4.2　结果分析

#### 4.2.1　目视比较

与原始的图像相比较，纠正后图像的地形效应基本被去除。原始图像山区阴坡和阳坡的色调差异大，整幅图像的立体感强，起伏明显，同种地物阴阳坡的反射率差异造成的异物同谱现象严重。纠正后的整幅图像辐射亮度较为均匀，阴阳坡灰度差异有所减小，空间立体感大大削弱。由于图像成像天顶角较大，整体纠正效果明显，但在部分阴坡存在过纠正。高亮度区域地形纠正的效果较好，但在山势陡峭坡度较大的地区以及遮蔽效应严重的区域，纠正效果不够理想。

#### 4.2.2　直方图与统计数据比较

通过多种统计参数可以定量的分析纠正后遥感图像的质量。定量评价遥感影像的统计参数较多，大多用图像最大值、最小值、均值、标准差 4 个参数评价阴影区域信息恢复程度和纠正前后影像光谱特性的保持程度。从表 2 中看出，各波段的均值有所增加，标准差有所减小，说明纠正方法恢复了处在阴影处像元的辐射亮度。

图像直方图描述图像中各像元的亮度统计分布。图 6 显示了 TM 各波段纠正前后图像直方图的变化。4 个波段纠正后的直方图近似高斯分布，与自然地物亮度随机特性相一致，反映了该地区地物真实统计特性，有效地去除了地形的影响。但是 TM3、TM4 波段阴坡的像元没有完全被恢复，低亮度值偏多。

#### 4.2.3　分类结果比较

地形纠正前的地物由于阴坡阳坡辐射亮度差异明显，导致分类结果受地形影响明显。纠正后图像的分类结果则与目视效果更加一致，更多的反映了地表实际分布情况。本文利用非监督分类方法对原始图像和经过地形纠正的图像进行了分类，一类为植被，另一类为非植被地，如图 7。

从图像上选取处于阴影区和光照区的植被和非植被地，分成阴坡植被、阳坡植被、阴坡非植被和阳坡非植被 4 个地物类别，计算每一类地物在不同波段纠正前后辐射亮度变化，如表 3。可以看出，相对于原始影像，纠正后的阴坡像元平均辐射亮度增加，而阳坡像元平均辐射亮度减小，同类地物辐射

表 2　纠正前后各波段统计参数表　/(W·m$^{-2}$·sr$^{-1}$)

| 波段 | 原始影像 | | | | 纠正后影像 | | | |
|---|---|---|---|---|---|---|---|---|
| | 最小值 | 最大值 | 均值 | 标准差 | 最小值 | 最大值 | 均值 | 标准差 |
| 1 | 29.58 | 65.61 | 36.31 | 3.20 | 32.58 | 71.18 | 38.98 | 2.35 |
| 2 | 14.46 | 68.83 | 26.48 | 5.72 | 16.88 | 76.93 | 30.12 | 4.26 |
| 3 | 7.31 | 81.10 | 25.33 | 8.87 | 8.13 | 67.53 | 28.39 | 6.89 |
| 4 | 2.38 | 66.68 | 24.95 | 11.57 | 3.02 | 68.98 | 27.22 | 7.67 |

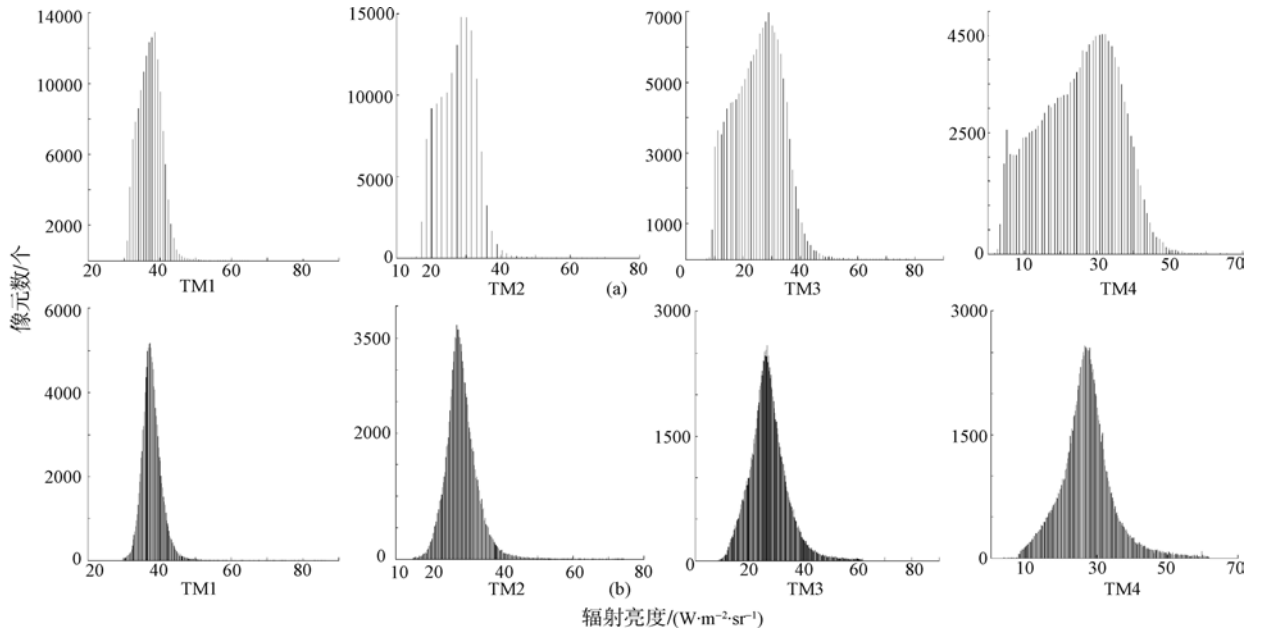


图 6　地形纠正前后各波段直方图对比

(a)原始图像直方图; (b)纠正后影像直方图

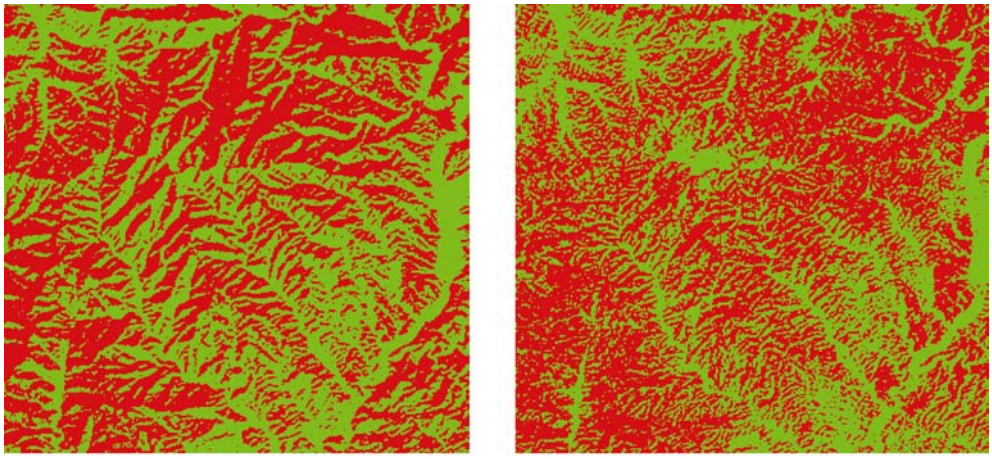

(a)　(b)

图 7　非监督分类结果

(a)原始图像分类; (b)纠正后的图像分类 (图中红色代表植被，绿色代表非植被地)

表 3　纠正前后各波段两类地物辐射亮度平均数值表　/(W·m$^{-2}$·sr$^{-1}$)

| 波段 | 植被 | | | | 非植被 | | | |
|---|---|---|---|---|---|---|---|---|
| | 纠正前 | | 纠正后 | | 纠正前 | | 纠正后 | |
| | 阳坡 | 阴坡 | 阳坡 | 阴坡 | 阳坡 | 阴坡 | 阳坡 | 阴坡 |
| 1 | 38.26 | 33.58 | 36.23 | 38.92 | 38.45 | 32.96 | 36.72 | 37.21 |
| 2 | 30.32 | 20.85 | 25.92 | 27.24 | 32.17 | 18.12 | 26.33 | 28.34 |
| 3 | 29.15 | 14.61 | 22.12 | 24.78 | 31.28 | 11.61 | 23.97 | 23.36 |
| 4 | 38.02 | 9.02 | 25.98 | 27.23 | 38.59 | 7.12 | 25.47 | 22.56 |

亮度趋于一致。

表 4 为选取不同光照系数(cosi)，植被和非植被区域地形纠正前后的光谱值。各种光照系数植被和非植被区纠正后光谱值有增有减，但相对纠正前辐射亮度更为接近，说明此方法有效地纠正了山地地形。在植被覆盖区，光照系数小的区域纠正后辐射亮度增加；光照系数大的区域，纠正后辐射亮度减小。纠正后图像 TM1—TM3 波段结果较好，辐射亮度趋于一致。第 4 波段特别是光照不足的植被区，光照系数较小时光谱值与其他系数的光谱值差距较大，存在一定的欠纠正。在非植被区，光照系数较小时纠正后光谱值增加明显，此处的地形处于阴坡，纠正后存在明显的过纠正现象。纠正后图像的过纠正和欠纠正现象产生原因主要有：对应区域的数字高程模型精度或配准精度不高，以及反演造成的大气参数误差。

#### 4.2.4　误差估计

由于物理模型的机理复杂，新模型建立进行的假设和近似方法的采用带来的误差在所难免。本文在求取气溶胶光学厚度时采用了暗目标法。Iqnatov 等在暗目标提取光学厚度可能引起的误差方面进行了讨论(Vermote 等，1997)，从理论上估计，当光学厚度较小时，误差在 5%—10%，光学厚度较大时，误差达到 20%。本文所选区域属于空气清洁的山区，光学厚度较小，取误差在 8%，光学厚度所在范围如表 5。

选第 1 波段做进一步的误差分析，把气溶胶光学厚度存在的范围带入 6S，得到 TM1 波段的参数见表 6。

表 4　纠正前后两类地物特征光照系数辐射亮度平均数值表　/(W·m$^{-2}$·sr$^{-1}$)

| 波段 | | 1 | | 2 | | 3 | | 4 | |
|---|---|---|---|---|---|---|---|---|---|
| 光照系数 | | 纠正前 | 纠正后 | 纠正前 | 纠正后 | 纠正前 | 纠正后 | 纠正前 | 纠正后 |
| 植被 | 0.1 | 33.93 | 36.06 | 19.31 | 26.12 | 12.67 | 23.81 | 8.54 | 22.70 |
| | 0.5 | 35.01 | 36.63 | 25.82 | 26.80 | 23.89 | 24.72 | 23.77 | 24.59 |
| | 0.9 | 38.25 | 36.17 | 31.19 | 26.09 | 31.96 | 24.81 | 38.04 | 26.11 |
| 非植被 | 0.1 | 34.66 | 41.97 | 22.03 | 35.81 | 16.76 | 35.55 | 12.22 | 33.71 |
| | 0.5 | 39.28 | 39.49 | 30.51 | 31.44 | 30.69 | 31.65 | 28.11 | 30.87 |
| | 0.9 | 43.24 | 40.61 | 36.2 | 32.93 | 31.8 | 30.19 | 40.22 | 29.11 |

表 5　第 1 波段光学厚度所在范围

| | TM1 | TM2 | TM3 | TM4 |
|---|---|---|---|---|
| 气溶胶光学厚度范围 | 0.16836—0.19764 | 0.14168—0.16632 | 0.11868—0.13932 | 0.092—0.108 |

表 6　TM1 的参数所在范围

| | 平均值 | 最低值 | 最高值 |
|---|---|---|---|
| 气溶胶光学厚度 | 0.183 | 0.16836 | 0.19764 |
| 程辐射/($W\cdot m^{-2}\cdot sr^{-1}$) | 29.58 | 29.021 | 30.135 |
| $k$ 值 | 0.2568 | 0.2753 | 0.2381 |

带入地形纠正程序，暗目标法对纠正后辐亮度结果的影响。

均值为 38.98$W\cdot m^{-2}\cdot sr^{-1}$，误差造成的均值所在区间为 38.56—39.43 $W\cdot m^{-2}\cdot sr^{-1}$(表 6)。

## 5　结　论

本文提出了一种专门针对地形效应的纠正方法。纠正模型基于辐射传输方程，对比经验纠正方法更为可靠，同时通过合理的近似和方程简化，避免了常规物理模型方程复杂、输入参数多等缺点。

对纠正后图像的统计数据、直方图以及分类数据的分析表明，本文的方法实现了对卫星遥感数据辐射亮度的纠正，消除了地形的影响，从目视效果来看，也说明了这种方法的有效性。由于本方法不需要同步的大气测量参数，通过引入漫散射辐射与直射辐射比例因子的概念，减少了需要从图像本身反演的参数个数，对于解决地形纠正的欠定问题有利，同时提高了地形纠正本身的可靠性，为山区遥感图像的进一步处理提供了便利。

## REFERENCES


Collins J B and Woodcock C E. 1996. An assessment of several linear change detection techniques for mapping forest mortality using multi-temporal Landsat TM data. *Remote Sens. Environ*, **56**: 66—77

Dozier J and Frew J. 1990. Rapid calculation of terrain parameters for radiation modeling from digital elevation data. *IEEE Trans. Geosci. Remote Sens*, **28**: 963—969

Franklin J, Logan T L, Woodcock C E and Strahler A H. 1986. Coniferous forest classification and inventory using Landsat and digital terrain data. *IEEE Trans. Geosci. Remote Sens*, **24**(1): 139—149

Hill J and Sturm B. 1991. Radiometric. correction of multi-temporal thematic mapper data for use in agricultural land-cover classification and vegetation monitoring. *Int. J. Remote Sens*, **12**: 1471—1491

Itten K I and Meyer P. 1993. Geometric and radiometric correction of TM data of mountainous forested areas. *IEEE Trans. Geosci. Remote Sensing*, **31**: 764—770

King M D, Kaufman Y J, Tanre D and Nakajima T. 1999. Remote sensing of tropospheric aerosols from spcace: past, present, and future. *Bulletin of the American Meteorological Society*, **80**: 2229—2259

Olsson H. 1995. Reflectance calibration of thematic mapper data for forest change detection. *Int. J. Remote Sensing*, **16**: 81—96

Proy C, Tanre D and Deschampls P Y. 1989. Evaluation of topographic effects in remotely sensed data. *Remote Sens. Environ*, **30**: 21—32

Remer L A, Kaufman Y J, Tanre D and Matto S. 2005. The MODIS aerosol algorithm, products, and validation. *Journal of the Atmospheric Sciences*, **62**(4): 947—927

Richter R. 1996a. A spatially adaptive fast atmospheric correction algorithm. *International Journal of Remote Sensing*, **17**: 1201—1214

Richter R. 1996b. Atmospheric correction of satellite data with haze removal including a haze/clear transition region. *Computers & Geosciences*, **22**: 675—681

Schaaf C B, Li X and Strahler A H. 1994. Topographic effects on bidirectional and hemispherical reflectances calculated with a geometric-optical canopy model. *IEEE Trans.Geosci. Remote Sensing*, **32**: 1186—1193

Vermote E F, Tanre D J, Deuze L, Herman and Morcrette J. 1997. Second simulation of the satellite signal in the solar spectrum, 6S: an overview. *IEEE Trans. Geosci. Remote Sens*, **35**: 675—686

Wang X Q, Yang S Z, Zhu Y H and Yi W N. 2003. Aerosol optical thickness retrieval over land from MODIS data based on the inversion of the 6S model. *Chinese Journal of Quantum Electronics*, **20**(5): 629—634

Yan G J, Zhu C G, Guo J, Wang J D and Li X W. 2000. A model based radiative transfer algorithm to correct remotely sensed image in mountainous area. *Journal of Image and Graphics*, (1): 11—15

Zhao C J, Song X Y, Wang J H, Liu L Y and Li C J. 2007. An algorithm based on 6S model for removing atmospheric effects form satellite imagery pixel by pixel. *Optical Technique*, **33**(1): 11—15

Zheng W and Zeng Z Y. 2004. A review on methods of atmospheric correction for remote sensing images. *Remote Sensing Information*, **4**: 66—67

Zhong Y W, Liu L Y, Wang J H and Yan G J. 2006. A method based on moment matching algorithm to correct remotely sensed image in rugged area. *Geography and Geo - Information Science*, **1**: 31—34


### 附中文参考文献


王新强，杨世植，朱永豪，易维宁. 2003. 基于 6S 模型从 MODIS 图像反演陆地上空大气气溶胶光学厚度. 量子电子学报, **20**(5): 629—634

阎广建，朱重光，郭军，王锦地，李小文. 2000. 基于模型的山地遥感图像辐射订正方法. 中国图形图像学报, (1): 11—15

赵春江，宋晓宇，王纪华，刘良云，李存军. 2007. 基于 6S 模型的遥感影像逐像元大气校正算法. 光学技术, **33**(1): 11—15

郑伟，曾志远. 2004. 遥感图像大气校正方法综述. 遥感信息，**4**: 66—67

钟耀武，刘良云，王纪华，阎广建. 2006. 基于局匹配算法的山区影像地形辐射方法研究. 地理与地理信息科学, **1**: 31—34